



Article

Fractional Temperature-Dependent BEM for Laser Ultrasonic Thermoelastic Propagation Problems of Smart Nanomaterials

Mohamed Abdelsabour Fahmy

Adham University College, Umm Al-Qura University, Adham, Makkah 28653, Saudi Arabia;
maselim@uqu.edu.sa; Tel.: +966-537930306

Abstract: The major goal of this work is to present a novel fractional temperature-dependent boundary element model (BEM) for solving thermoelastic wave propagation problems in smart nanomaterials. The computing performance of the suggested methodology was demonstrated by using stable communication avoiding S-step—generalized minimal residual method (SCAS-GMRES) to solve discretized linear BEM systems. The benefits of SCAS-GMRES are investigated and compared to those of other iterative techniques. The numerical results are graphed to demonstrate the influence of fractional, piezoelectric, and length scale characteristics on total force-stresses. These findings also demonstrate that the BEM methodology is practical, feasible, effective, and has superiority over domain methods. The results of the present paper help to develop the industrial uses of smart nanomaterials.

Keywords: fractional-order; temperature-dependent; size-dependent; boundary element method; thermoelastic problems; smart nanomaterials



Citation: Fahmy, M.A. Fractional Temperature-Dependent BEM for Laser Ultrasonic Thermoelastic Propagation Problems of Smart Nanomaterials. *Fractal Fract.* **2023**, *7*, 536. <https://doi.org/10.3390/fractalfract7070536>

Academic Editors: Mohammad Partohaghighi and Ali Akgül

Received: 15 June 2023

Revised: 6 July 2023

Accepted: 8 July 2023

Published: 11 July 2023



Copyright: © 2023 by the author. Licensee MDPI, Basel, Switzerland. This article is an open access article distributed under the terms and conditions of the Creative Commons Attribution (CC BY) license (<https://creativecommons.org/licenses/by/4.0/>).

1. Introduction

The fractional derivative, which is a generalization of the integer-order derivative and integral, is used to describe non-local behaviors and anomalous complex systems. In recent years, fractional heat equations have been proposed as generalizations of integer order heat equations. The flexibility and non-locality of fractional derivatives are their key features. Because these derivatives are of fractional order, they have greater flexibility in approximating real data than classical derivatives. Furthermore, they take non-locality into account, while classical derivatives do not, i.e., classical derivatives can only describe changes about a point, whereas fractional derivatives can describe changes in an interval. Fractional derivatives are nonlocal in nature. Because of this characteristic, these derivatives can be used to replicate other physical phenomena. In real life, fractional differential equations are used in control systems, elasticity, electric drives, circuit systems, continuum mechanics, heat transfer, quantum physics, fluid mechanics, signal analysis, biomathematics, biomedicine, social systems, and bioengineering.

Many studies in recent years have investigated the thermoelastic behavior of materials [1–6] due to their potential in geological and engineering applications. Nanotechnology is concerned with developing tools for studying the properties of nanomaterials, whereas nanoscience is concerned with moving and manipulating atoms to achieve the properties required in a particular field of life [7,8]. Nanostructures are one of the most important outcomes of nanotechnology. A structure is classified as a nanostructure if one of its dimensions is 100 nanometers or less. Understanding the mechanical behavior of deformed nanostructures is critical because they are used in a wide range of industries and professions, including engineering, medicine, renewable energy, and military applications. In the industrial sector, certain nanoparticles are used to create filters due to their greater strength as compared to traditional materials [9]. Because of recent advances in nanoscale electronics and photonics [10–12], certain nanoparticles can be utilized as drug-carrying materials

in the medical profession because they have a unique sensitivity to the place inside the human body to which the drug is supposed to be conveyed. When they reach that location, they accurately release the drug. Encouragement studies have also confirmed the potential for employing nanoparticles as a cancer treatment. Furthermore, gold nanoparticles are employed to detect pregnancies in home pregnancy test kits. Nanowires are being employed in nanoscale biosensors for early illness detection [13,14]. In the field of renewable energy, the panel, which is connected by an electrical circuit and contains hundreds of solar cells, converts solar energy into electrical energy. Military uses for nanomaterials include the creation of nanoscale cylinders with strength and rigidity that have a million times the storage capacity of conventional computers, military clothing that can absorb radar waves for stealth and infiltration, and nanosatellites [15–17]. Specific nanomaterials are incorporated into concrete in the building and construction industry to improve its tenacity, rigor, and water resistance. These materials include silica nanoparticles, carbon nanotubes, and titanium dioxide (TiO₂). Many nanotechnology applications rely on porothermoelastic interactions that vary with size [18–20]. Because size-dependent thermopiezoelectric problems are computationally complex to solve and do not have a general analytical solution, numerical methods for solving them should be developed [21]. The BEM model of Fahmy et al. [22] described the thermopiezoelectricity theory in smart nanomaterials. In the BEM model considered herein, we introduce a new solution for fractional, temperature-dependent, and wave propagation size-dependent thermopiezoelectricity problems in smart nanomaterials. This paper may be considered as an extension of [22], with fractional, temperature-dependent, and wave propagation effects that are not considered in [22]. The boundary element method (BEM) is an efficient numerical approach employed to solve partial differential equations [23–26]. It outperforms the finite element method (FEM) in several ways [27]. Only the problem's boundary needs to be discretized for the BEM. In comparison to FEM, which necessitates discretization of the entire problem domain, it has a substantial advantage. Because it requires less computational work and input data preparation, this feature is critical for solving complex problems in smart nanomaterials. It also improves the feature's usability. Only the BEM formulation procedure can address infinite domain problems with complicated borders and geometrical quirks accurately. The BEM approach is particularly effective for measuring field derivatives such as tractions, heat fluxes, and sensitivities. The BEM solution is provided by the integral representation expression. In the FEM, the solution is only computed at nodal points. As a result, the BEM has recently emerged as a reliable, practical, and widely used alternative to FEM for modelling of fractional temperature- and size-dependent thermoelastic problems in smart nanomaterial technology.

In this paper, the temperature-dependent thermoelasticity problems are solved using the boundary element method (BEM) to understand the mechanical characteristics of deformed smart nanomaterials. The numerical results show the impacts of the fractional parameter, piezoelectric parameter, and length-scale parameter on the total force-stresses. The numerical results also show temperature-dependent and temperature-independent effects on smart nanomaterials and non-smart nanomaterials, as well as the viability, effectiveness, and precision of the current BEM methodology.

2. Formulation of the Problem

Consider a cross section of thermoelastic smart nanomaterial in the x_1x_2 – plane, occupying the region V that is bounded by S , as shown in Figure 1. Assume n_α can be written as

$$n_\alpha = e_{\alpha\beta} \frac{dx_\beta}{ds} \quad (1)$$

where $e_{\alpha\beta}$ ($e_{12} = -e_{21} = 1$, $e_{11} = e_{22} = 0$).

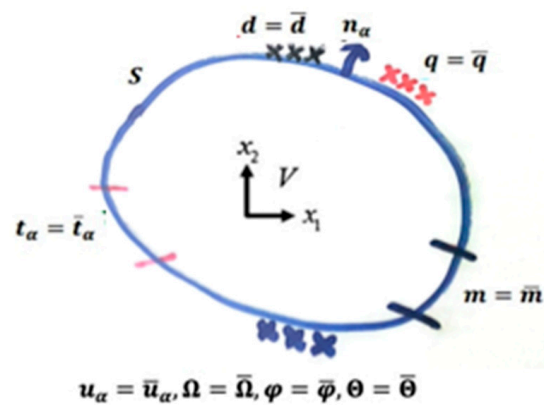


Figure 1. Size-dependent thermoelastic smart nanomaterial.

All quantities in the x_1x_2 – plane are independent of x_3 .

The rotation in terms of deformation displacement vector (u_1, u_2) and electric field in terms of electric potential φ can be expressed as

$$\Omega = \Omega_3 = \frac{1}{2}(u_{2,1} - u_{1,2}) = \frac{1}{2}e_{\alpha\beta}u_{\beta,\alpha} \quad (2)$$

$$E_\alpha = -\varphi_{,\alpha} \quad (3)$$

The strain tensor, mean curvature vector, and true couple-stress can be written as follows:

$$\varepsilon_{\alpha\beta} = \frac{1}{2}(u_{\alpha,\beta} + u_{\beta,\alpha}) \quad (4)$$

$$k_\alpha = e_{\alpha\beta}k_{3\beta} = \frac{1}{2}e_{\alpha\beta}\Omega_{,\beta} \quad (5)$$

$$M_i = \frac{1}{2}e_{ijk}M_{kj} \quad (6)$$

where $k_1 = k_{32} = \frac{1}{2}\Omega_{,2}$, $k_2 = -k_{31} = -\frac{1}{2}\Omega_{,1}$, and $k_{3\alpha} = -k_{\alpha 3} = \frac{1}{2}\Omega_{,\alpha}$, $M_\alpha = \varepsilon_{\alpha\beta}M_{3\beta}$, $M_{ij} = -M_{ji}$, $M_1 = -M_{23}$, $M_2 = M_{13}$, and $M_3 = M_{21} = 0$. The force-stress tensor can be divided into two sections:

$$\sigma_{\alpha\beta} = \sigma_{(\alpha\beta)} + \sigma_{[\alpha\beta]}, \quad \sigma_{3\alpha} = \sigma_{\alpha 3} = 0 \quad (7)$$

The electric displacement D_α is given as

$$D_\alpha = e_0E_\alpha + P_\alpha \quad (8)$$

The governing equations for entropy balance, force equilibrium, moment equilibrium equations, and Gauss's law for the electric field of the considered smart nanomaterial can be expressed as

$$-q_{\alpha,\alpha} + Q = 0 \quad (9)$$

$$\sigma_{\beta\alpha,\beta} + F_\alpha = 0 \quad (10)$$

$$\sigma_{[\beta\alpha]} = -M_{[\alpha,\beta]}, \quad \sigma_{[21]} = -\sigma_{[12]} = -M_{[1,2]} \quad (11)$$

$$D_{\alpha,\alpha} = \rho_E \quad (12)$$

$$\left[\sigma_{(\beta\alpha)} - M_{[\alpha, \beta]} \right]_{,\beta} + F_\alpha = 0 \quad (13)$$

Now, we present the following constitutive equations of the considered smart nanomaterial. The heat flux is

$$q_\alpha = -k\Theta_{,\alpha} \quad (14)$$

The force-stress, couple-stress, and electric displacement are

$$\sigma_{(\alpha\beta)} = \lambda \varepsilon_{\gamma\gamma} \delta_{\alpha\beta} + 2\mu \varepsilon_{\alpha\beta} - (3\lambda + 2\mu) \bar{\alpha} \Theta \delta_{\alpha\beta} \quad (15)$$

$$M_\alpha = -8\mu l^2 k_\alpha + 2f E_\alpha, \quad l^2 = \frac{\eta}{\mu} \quad (16)$$

$$D_\alpha = e E_\alpha + 4f k_\alpha \quad (17)$$

The force-traction, couple-traction, and normal electric displacement are

$$t_\alpha = \sigma_{\beta\alpha} n_\beta \quad (18)$$

$$m = e_{\beta\alpha} M_\alpha n_\beta = M_2 n_1 - M_1 n_2 \quad (19)$$

$$d = D_\alpha n_\alpha \quad (20)$$

Thus, the total force-stress tensor is

$$\sigma_{\beta\alpha} = \lambda \varepsilon_{\gamma\gamma} \delta_{\alpha\beta} + 2\mu \varepsilon_{\alpha\beta} + 2\mu l^2 e_{\alpha\beta} \nabla^2 \Omega - \frac{E}{1-2\nu} \bar{\alpha} \Theta \delta_{\alpha\beta} \quad (21)$$

where

$$E = 2\mu(1+\nu), \quad \lambda = 2\mu \frac{\nu}{1-2\nu}$$

The fractional-order temperature-dependent heat equation is

$$D_\tau^\alpha \Theta(\mathbf{x}, \tau) = \zeta \nabla [\lambda(\Theta) \nabla \Theta(\mathbf{x}, \tau)] + \zeta Q(\mathbf{x}, \Theta, \tau), \quad \zeta = \frac{1}{\rho(\Theta) c(\Theta)} \quad (22)$$

in which

$$Q(\mathbf{x}, \Theta, \tau) = \bar{Q}(\mathbf{x}, \Theta, \tau) + \frac{1-R}{\mathbf{x}_0} e^{(-\frac{\mathbf{x}_a}{\mathbf{x}_0})J(\tau)}, \quad J(t) = \frac{J_0 \tau}{\tau_1^2} e^{-\frac{\tau}{\tau_1}}, \quad a = 1, 2, 3$$

As a result, Equations (9), (10), and (12) may be expressed as

$$k \nabla^2 \Theta + Q = 0 \quad (23)$$

$$\lambda u_{\beta,\beta\alpha} + \mu \left((1 + l^2 \nabla^2) u_{\beta,\beta\alpha} + (1 - l^2 \nabla^2) \nabla^2 u_\alpha \right) - \frac{E}{1-2\nu} \bar{\alpha} \Theta_{,\alpha} + F_\alpha = 0 \quad (24)$$

$$e \nabla^2 \varphi + \rho_E = 0, \quad e = e_r e_0 \quad (25)$$

Now, we can introduce the following definitions for q , t_α , m , and d , as follows. The normal heat flux is

$$q = q_\alpha n_\alpha = -k \frac{\partial \Theta}{\partial n} \quad (26)$$

The force-traction vector is

$$t_\alpha = \sigma_{\beta\alpha} n_\beta = \left(\lambda \varepsilon_{\gamma\gamma} \delta_{\alpha\beta} + 2\mu \varepsilon_{\alpha\beta} + 2\mu l^2 e_{\alpha\beta} \nabla^2 \Omega - \frac{E}{1-2\nu} \bar{\alpha} \Theta \delta_{\alpha\beta} \right) n_\beta \quad (27)$$

The couple-traction is

$$m = e_{\beta\alpha} \mu_\alpha n_\beta = 4\mu l^2 \frac{\partial \Omega}{\partial n} - 2f \frac{\partial \varphi}{\partial s} \quad (28)$$

The normal electric displacement is

$$d = D_\alpha n_\alpha = -e \frac{\partial \varphi}{\partial n} + 2f \frac{\partial \Omega}{\partial s} \quad (29)$$

3. Boundary Conditions

The temperature and displacement boundary conditions under consideration are

$$\Theta = \bar{\Theta} \text{ on } S_T \quad (30)$$

$$q = \bar{q} \text{ on } S_q, S_T \cup S_q = S, S_T \cap S_q = \emptyset \quad (31)$$

$$u_\alpha = \bar{u}_\alpha \text{ on } S_u \quad (32)$$

$$t_\alpha = \bar{t}_\alpha \text{ on } S_t, S_u \cup S_t = S, S_u \cap S_t = \emptyset \quad (33)$$

where

$$\Omega = \bar{\Omega} \text{ on } S_\omega \quad (34)$$

$$m = \bar{m} \text{ on } S_m, S_\omega \cup S_m = S, S_\omega \cap S_m = \emptyset \quad (35)$$

and

$$\varphi = \bar{\varphi} \text{ on } S_\varphi \quad (36)$$

$$d = \bar{d} \text{ on } S_d, S_\varphi \cup S_d = S, S_\varphi \cap S_d = \emptyset \quad (37)$$

where $S_T, S_q, S_u, S_t, S_\omega, S_m, S_\varphi$, and S_d are the specified boundary values for $T, q, u_\alpha, t_\alpha, \Omega, m, \varphi$, and d , respectively.

4. Boundary Element Implementation

By using Caputo's formula and Equation (22), we obtain the following [28,29]:

$$D_\tau^a \Theta^{f+1} + D_\tau^a \Theta^f \approx \sum_{J=0}^k W_{a,J} \left(\Theta^{f+1-J}(\mathbf{x}) - \Theta^{f-J}(\mathbf{x}) \right) \quad (38)$$

where

$$W_{a,0} = \frac{(\Delta\tau)^{-a}}{\Gamma(2-a)} \text{ and } W_{a,J} = W_{a,0} \left((J+1)^{1-a} - (J-1)^{1-a} \right) \quad (39)$$

By using Equation (38), Equation (22) may be written as

$$\begin{aligned} & W_{a,0} \Theta^{f+1}(\mathbf{x}) - \lambda(\mathbf{x}, \Theta) \Theta_{,ii}^{f+1}(\mathbf{x}) - \lambda_{,i}(\mathbf{x}, \Theta) \Theta_{,i}^{f+1}(\mathbf{x}) \\ & = W_{a,0} \Theta^f(\mathbf{x}) - \lambda(\mathbf{x}) \Theta_{,ii}^f(\mathbf{x}) - \lambda_{,i}(\mathbf{x}, \Theta) \Theta_{,i}^f(\mathbf{x}) - \sum_{j=1}^f W_{a,j} \left(\Theta^{f+1-j}(\mathbf{x}) - \Theta^{f-j}(\mathbf{x}) \right) + h_m^{f+1}(\mathbf{x}, \Theta, \tau) + h_m^f(\mathbf{x}, \Theta, \tau) \end{aligned} \quad (40)$$

By using the Kirchhoff transformation, $T = \int_{T_0}^T \frac{\lambda(\Theta)}{\lambda_0} d\Theta$. [30], Equation (22) may be written as follo [31]:

$$\nabla^2 T(\mathbf{x}, \tau) + \frac{1}{\lambda_0} h(\mathbf{x}, T, \tau) = \frac{\rho_0 c_0}{\lambda_0} \frac{\partial T(\mathbf{x}, \tau)}{\partial \tau} + NI(\mathbf{x}, T, \dot{T}) \quad (41)$$

which can be expressed as [31]

$$\nabla^2 T(\mathbf{x}, \tau) + \frac{1}{\lambda_0} h_{NI}(\mathbf{x}, T, \dot{T}, \tau) = \frac{\rho_0 c_0}{\lambda_0} \frac{\partial T(\mathbf{x}, \tau)}{\partial \tau} \quad (42)$$

in which

$$NI(\mathbf{x}, T, \dot{T}) = \left[\frac{\rho(T) c(T)}{\lambda(T)} - \frac{\rho_0 c_0}{\lambda_0} \right] \dot{T} \quad (43)$$

$$h_{NI}(\mathbf{x}, T, \dot{T}, \tau) = h(\mathbf{x}, T, \tau) + \left[\rho_0 c_0 - \frac{\lambda_0}{\lambda(T)} \rho(T) c(T) \right] \dot{T} \quad (44)$$

The fundamental solution of (40) can be used to define the integral equation corresponding to (42) as follows [32]:

$$\begin{aligned} C(P)T(P, \tau_{n+1}) + a_0 \int_{\Gamma} \int_{\tau_n}^{\tau_{n+1}} T(Q, \tau) q^*(P, \tau_{n+1}; Q, \tau) d\tau d\Gamma \\ = a_0 \int_{\Gamma} \int_{\tau_n}^{\tau_{n+1}} q(Q, \tau) T^*(P, \tau_{n+1}; Q, \tau) d\tau d\Gamma + \frac{a_0}{\lambda_0} \int_{\Omega} \int_{\tau_n}^{\tau_{n+1}} h_{NI}(Q, T, \dot{T}, \tau) T^*(P, \tau_{n+1}; Q, \tau) d\tau d\Omega \\ + \int_{\Omega} T(Q, \tau_n) T^*(P, \tau_{n+1}; Q, \tau) d\Omega, \quad a_0 = \frac{\lambda_0}{\rho_0 c_0} \end{aligned} \quad (45)$$

By using the same technique of Fahmy [31], the radial point interpolation method (RPIM) and Cartesian transformation method (CTM) [33–36] are used to treat the domain integrals in Equation (45), which results from the fractional-order temperature-dependent heat conduction in Equation (22).

The boundary integral equations can now be expressed as follows [37–39]:

$$c^{Q^*}(\xi)T(\xi) - \int_S q^{Q^*}(\mathbf{x}, \xi)T(\mathbf{x})dS(\mathbf{x}) = - \int_S T^{Q^*}(\mathbf{x}, \xi)q(\mathbf{x})dS(\mathbf{x}) + \int_V T^{Q^*}(\mathbf{x}, \xi)Q(\mathbf{x})dV(\mathbf{x}) \quad (46)$$

$$\begin{aligned} c_{\alpha\beta}(\xi)u_{\alpha}(\xi) + \oint_S t_{\alpha\beta}^{F^*}(\mathbf{x}, \xi)u_{\alpha}(\mathbf{x})dS(\mathbf{x}) + \int_S m_{\beta}^{F^*}(\mathbf{x}, \xi)\Omega(\mathbf{x})dS(\mathbf{x}) + \int_S h_{\beta}^{F^*}(\mathbf{x}, \xi)T(\mathbf{x})dS(\mathbf{x}) + \int_S d_{\beta}^{F^*}(\mathbf{x}, \xi)\varphi(\mathbf{x})dS(\mathbf{x}) \\ = \int_S u_{\alpha\beta}^{F^*}(\mathbf{x}, \xi)t_{\alpha}(\mathbf{x})dS(\mathbf{x}) + \int_S \Omega_{\beta}^{F^*}(\mathbf{x}, \xi)m(\mathbf{x})dS(\mathbf{x}) + \int_V u_{\alpha\beta}^{F^*}(\mathbf{x}, \xi)F_{\alpha}(\mathbf{x})dV \\ + \int_S f_{\beta}^{F^*}(\mathbf{x}, \xi)q(\mathbf{x})dS(\mathbf{x}) - \int_V f_{\beta}^{F^*}(\mathbf{x}, \xi)Q(\mathbf{x})dV \end{aligned} \quad (47)$$

$$\begin{aligned} c^{\Omega}(\xi)\Omega(\xi) + \int_S t_{\alpha}^{C^*}(\mathbf{x}, \xi)u_{\alpha}(\mathbf{x})dS(\mathbf{x}) + \oint_S m^{C^*}(\mathbf{x}, \xi)\Omega(\mathbf{x})dS(\mathbf{x}) + \oint_S d^{C^*}(\mathbf{x}, \xi)\varphi(\mathbf{x})dS(\mathbf{x}) \\ = \int_S u_{\alpha}^{C^*}(\mathbf{x}, \xi)t_{\alpha}(\mathbf{x})dS(\mathbf{x}) + \int_S \Omega^{C^*}(\mathbf{x}, \xi)m(\mathbf{x})dS(\mathbf{x}) + \int_V u_{\alpha}^{C^*}(\mathbf{x}, \xi)F_{\alpha}(\mathbf{x})dV \end{aligned} \quad (48)$$

$$\begin{aligned} c^{\varphi}(\xi)\varphi(\xi) + \oint_S m^{R^*}(\mathbf{x}, \xi)\Omega(\mathbf{x})dS(\mathbf{x}) + \oint_S d^{R^*}(\mathbf{x}, \xi)\varphi(\mathbf{x})dS(\mathbf{x}) \\ = \int_S \varphi^{R^*}(\mathbf{x}, \xi)d(\mathbf{x})dS(\mathbf{x}) - \int_V \varphi^{R^*}(\mathbf{x}, \xi)\rho_E(\mathbf{x})dV \end{aligned} \quad (49)$$

The integral Equations (46)–(49) in the absence of body forces and volume charge density can be written in matrix form as follows:

$$\begin{bmatrix} c^{\mathcal{Q}^*}(\xi)T(\xi) \\ c_{\alpha\beta}^{\omega}(\xi)u_{\alpha}(\xi) \\ c^{\omega}(\xi)\Omega(\xi) \\ c^{\phi}(\xi)\varphi(\xi) \end{bmatrix} + \oint_S \begin{bmatrix} -q^{\mathcal{Q}^*} & 0 & 0 & 0 \\ h_{\beta}^{F^*} & t_{\alpha\beta}^{F^*}(x, \xi) & m_{\beta}^{F^*}(x, \xi) & d_{\beta}^{F^*}(x, \xi) \\ 0 & t_{\alpha}^{C^*}(x, \xi) & m^{C^*}(x, \xi) & d^{C^*}(x, \xi) \\ 0 & 0 & m^{R^*}(x, \xi) & d^{R^*}(x, \xi) \end{bmatrix} \begin{bmatrix} T(x) \\ u_{\alpha}(x) \\ \Omega(x) \\ \varphi(x) \end{bmatrix} dS(x) \\ = \int_S \begin{bmatrix} -\vartheta^{\mathcal{Q}^*} & 0 & 0 & 0 \\ f_{\beta}^{F^*}(x, \xi) & u_{\alpha\beta}^{F^*}(x, \xi) & \Omega_{\beta}^{F^*}(x, \xi) & 0 \\ 0 & u_{\alpha}^{C^*}(x, \xi) & \Omega^{C^*}(x, \xi) & 0 \\ 0 & 0 & 0 & \varphi^{R^*}(x, \xi) \end{bmatrix} \begin{bmatrix} q(x) \\ t_{\alpha}(x) \\ m(x) \\ d(x) \end{bmatrix} dS(x) \quad (50)$$

Now, it is convenient to rewrite Equation (50) in compact index-notation form as

$$c_{IJ}(\xi)u_I(\xi) + \oint_S t_{IJ}^*(x, \xi)u_I(x)dS(x) = \int_S u_{IJ}^*(x, \xi)t_I(x)dS(x) \quad (51)$$

This leads to the following linear algebraic equations system:

$$\overline{T}\overline{u} = \overline{U}\overline{t} \quad (52)$$

which can also be expressed as

$$AX = B \quad (53)$$

5. Numerical Results and Discussion

To demonstrate the numerical computations calculated using the proposed methodology, we consider the temperature-dependent thermoelastic smart nanomaterial properties of pure copper (Cu) nanoparticles [40,41] as shown in Table 1 and using the boundary conditions depicted in Figure 2 to exemplify the numerical computations computed by the suggested methodology. Under thermal and piezoelectric loadings, the considered thermoelastic smart nanomaterial deforms and becomes electrically polarized. As illustrated in Figure 3, the BEM discretization used 42 border elements and 68 internal points.

Table 1. Considered properties of pure copper (Cu) nanoparticles [42].

T(°C)	0	500	900
C(J/kg) °K	385	433	480
ρ (kg/m ³)	8930	8686	8458

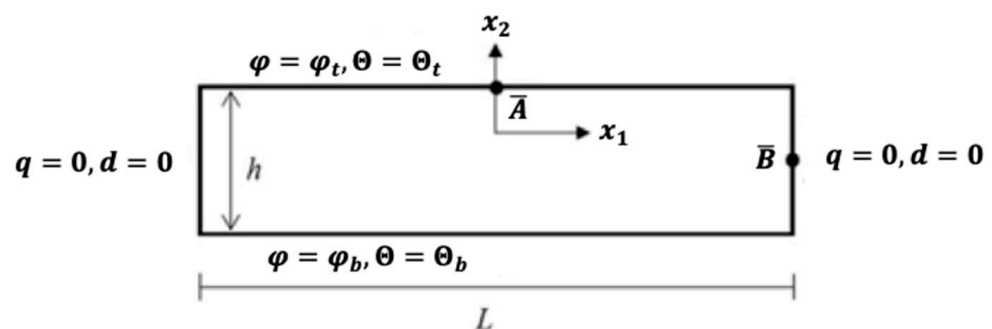


Figure 2. Geometry of the considered thermoelastic smart nanomaterial.

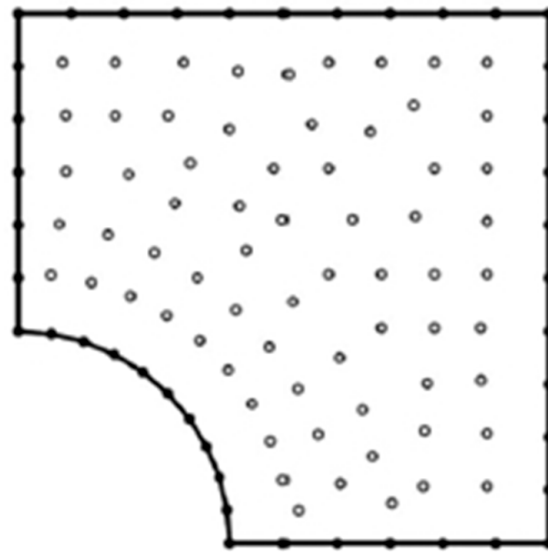


Figure 3. BEM model of the current problem.

The thermal conductivity of pure copper (Cu) nanoparticles is

$$\lambda = 400 \left(1 - \frac{T}{6000} \right)$$

The solid line indicates Case A, which represents temperature-dependent smart nanomaterials ($f = -1$). Case B is shown by the dashed line, which represents temperature-dependent non-smart nanomaterials ($f = 0$). The dotted line indicates Case C, which represents temperature-independent smart nanomaterials ($f = -1$). Case D is shown by the dash-dot line, which represents temperature-independent non-smart nanomaterials ($f = 0$).

In the present paper, to solve linear systems generated by BEM discretization efficiently, we used the stable communication avoiding S-step—generalized minimal residual method (SCAS-GMRES) of Zan et al. [43] to reduce the number of iterations and computation time. The SCAS-GMRES method [43], fast modified diagonal and toeplitz splitting (FMDTS) method of Xin and Chong [44], and unconditionally convergent—respectively scaled circulant and skew-circulant splitting (UC-RSCSCS) method of Zi et al. [45] were compared when considering the solution of the current problem, as shown in Table 2. This table shows the number of iterations (Iter.), processor time (CPU time), relative residual (Rr), and error (Err.) calculated for different length scale values. According to Table 2, the SCAS-GMRES iterative method requires the least amount of IT and CPU time, implying that it outperforms the FMDTS and UC-RSCSCS iterative methods.

Table 3 explains the numerical solutions obtained for total force-stress σ_{11} at points \bar{A} and \bar{B} for various length scale values ($l = 0.01, 0.1, \text{ and } 1.0$). Table 3 additionally provides the finite element method (FEM) data of Sladek et al. [46] and the analytical data of Yu et al. [47] for our investigated problem. As demonstrated in Table 3, the BEM data are very consistent with the FEM and analytical data. As a result, the proposed BEM's validity and precision are demonstrated.

From Figure 4, it is obvious that the total force-stress σ_{11} increases, decreases, then increases towards zero as x_1 tends toward infinity for different theories.

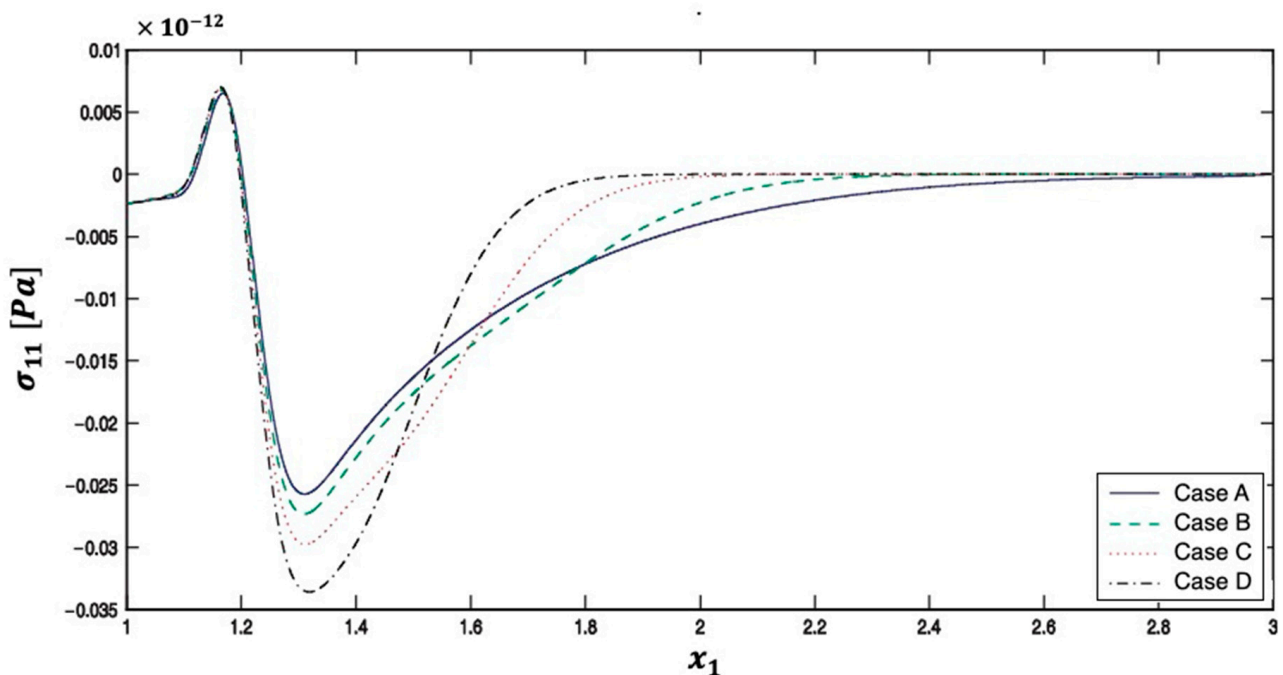
From Figure 5, it is obvious that the total force-stress σ_{12} decreases, increases, decreases, then increases towards zero as x_1 tends toward infinity for different theories.

Table 2. Results for the iteration techniques.

l	Method	Iter.	CPU Time	Rr	Err.
0.01	SCAS-GMRES	30	0.0119	1.96×10^{-7}	1.48×10^{-9}
	FMDTS	60	0.0564	5.50×10^{-7}	1.72×10^{-7}
	UC-RSCSCS	70	0.0730	7.02×10^{-7}	2.50×10^{-6}
0.1	SCAS-GMRES	40	0.0538	0.19×10^{-6}	2.06×10^{-8}
	FMDTS	90	0.2239	1.72×10^{-5}	4.52×10^{-6}
	UC-RSCSCS	120	0.3764	1.16×10^{-4}	0.58×10^{-5}
1.0	SCAS-GMRES	60	0.1758	2.22×10^{-5}	1.80×10^{-7}
	FMDTS	270	0.7940	1.80×10^{-4}	3.62×10^{-5}
	UC-RSCSCS	280	0.8950	1.22×10^{-3}	4.60×10^{-4}

Table 3. Numerical values for total force-stress σ_{11} at points \bar{A} and \bar{B} .

l	BEM		FEM		Analytical	
	$(\sigma_{11})_{\bar{A}}^-$	$(\sigma_{11})_{\bar{B}}^-$	$(\sigma_{11})_{\bar{A}}^-$	$(\sigma_{11})_{\bar{B}}^-$	$(\sigma_{11})_{\bar{A}}^-$	$(\sigma_{11})_{\bar{B}}^-$
0.01	-0.04766×10^{-12}	-0.01847×10^{-12}	-0.04769×10^{-12}	-0.01850×10^{-12}	-0.04767×10^{-12}	-0.01848×10^{-12}
0.1	-0.02452×10^{-12}	-0.02113×10^{-12}	-0.02455×10^{-12}	-0.02116×10^{-12}	-0.02453×10^{-12}	-0.02114×10^{-12}
1.0	-0.01984×10^{-12}	-0.02582×10^{-12}	-0.01987×10^{-12}	-0.02586×10^{-12}	-0.01985×10^{-12}	-0.02583×10^{-12}

**Figure 4.** Total force-stress σ_{11} distribution on x_1 -axis for various smart nanomaterial theories.

From Figure 6, it is obvious that the total force-stress σ_{11} increases, decreases, then increases towards zero as x_1 tends toward infinity. It is also shown that the total force-stress σ_{22} increases with small values of x_1 and then decreases and increases with large values of x_1 .

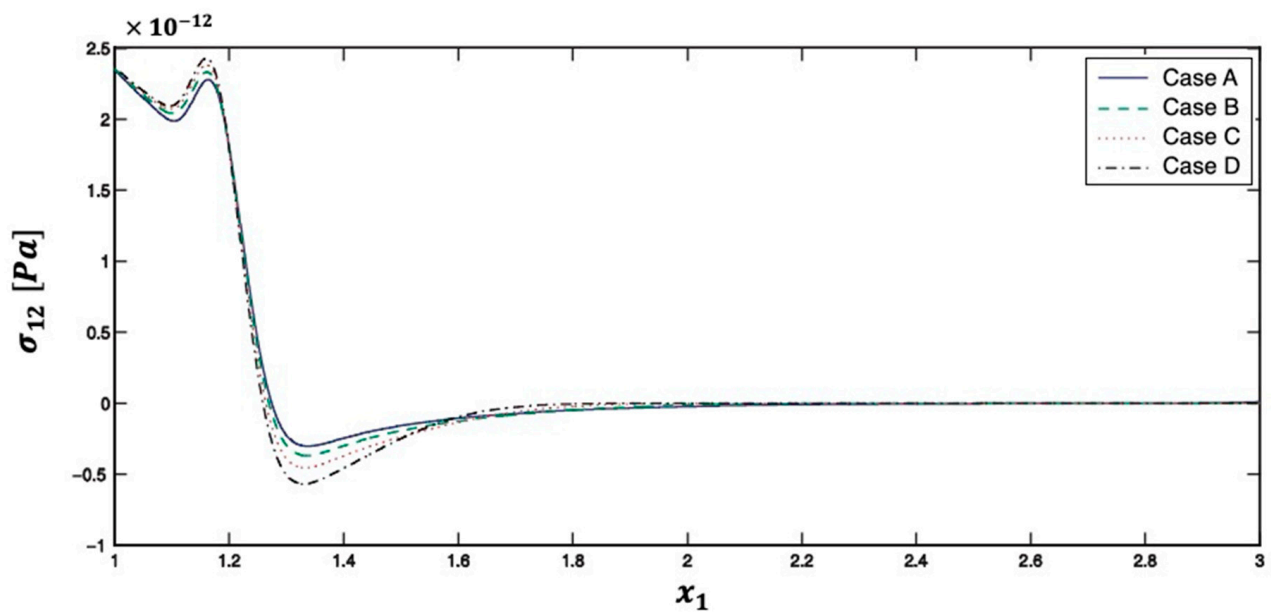


Figure 5. Total force-stress σ_{12} distribution on x_1 -axis for various smart nanomaterial theories.

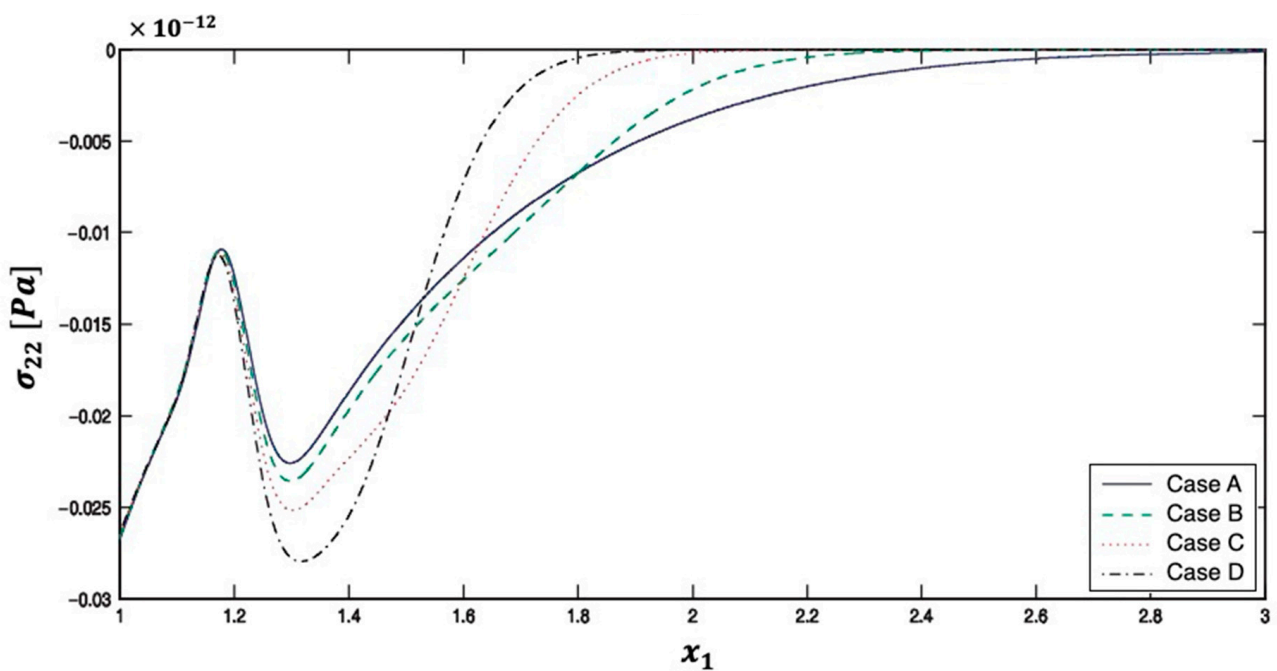


Figure 6. Total force-stress σ_{22} distribution on x_1 -axis for various smart nanomaterial theories.

From Figure 7, it is obvious that the total force-stress σ_{11} decreases with an increase of x_1 but increases with an increase of fractional order parameter a .

From Figure 8, it is clear that the total force-stress σ_{12} increases and decreases with an increase of x_1 and tends to zero as x_1 tends to infinity. It is also shown that the values of total force-stress σ_{12} almost coincide at the different values of fractional order parameter a , except for the interval $1.25 < x_1 < 2.20$, where we find that the total force-stress σ_{12} decreases with an increase of fractional order parameter a .

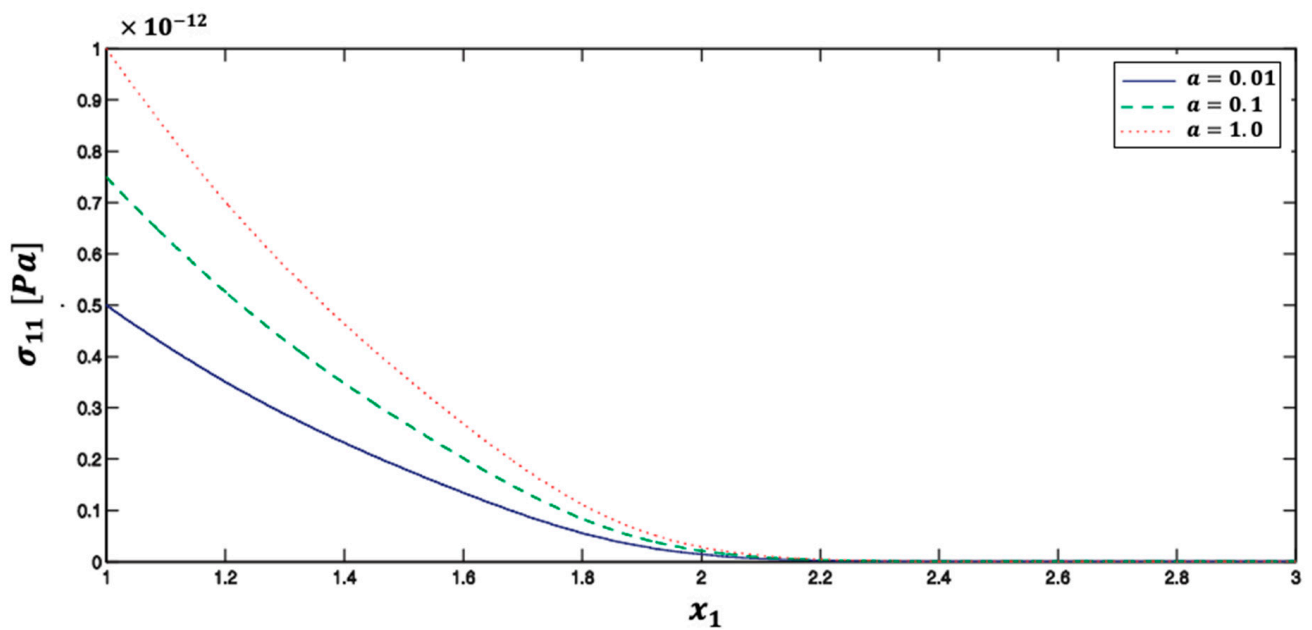


Figure 7. Total force-stress σ_{11} distribution on x_1 -axis for various fractional parameter a values.

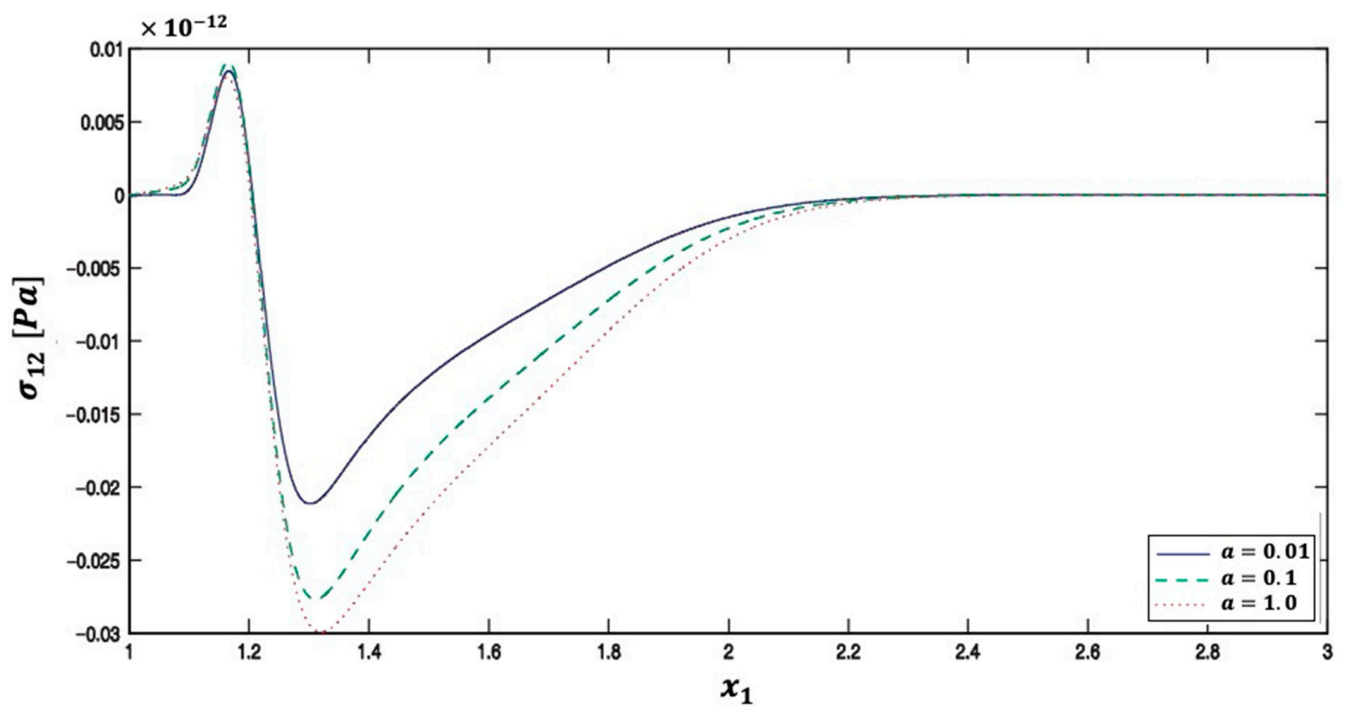


Figure 8. Total force-stress σ_{12} distribution on x_1 -axis for various fractional parameter a values.

From Figure 9, it is obvious that the total force-stress σ_{22} increases, decreases, and tends toward zero as x_1 tends toward infinity. It is also clear that the total force-stress σ_{22} decreases with the increase of fractional order parameter a .

From Figure 10, it is obvious that the total force-stress σ_{11} increases, decreases, and tend toward zero as x_1 tends to infinity. It is also clear that the total force-stress σ_{11} decreases with the increasing of piezoelectric parameter f .

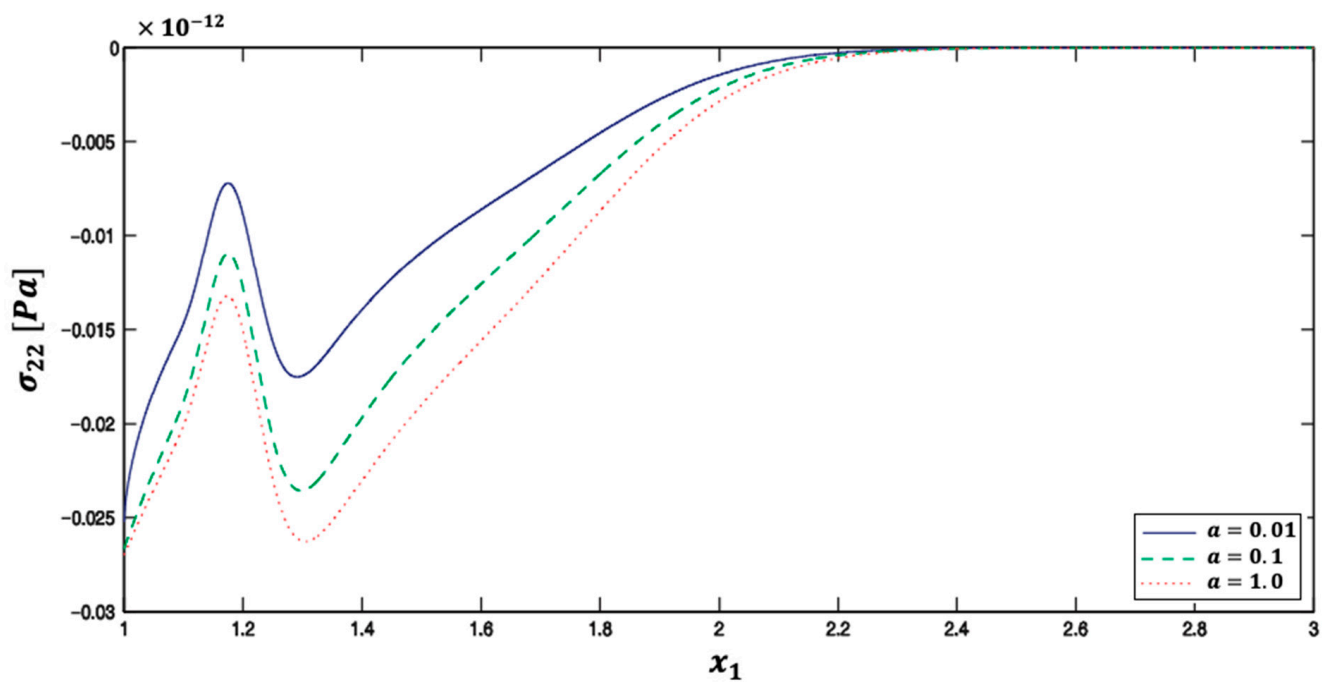


Figure 9. Total force-stress σ_{22} distribution on x_1 -axis for various fractional parameter a values.

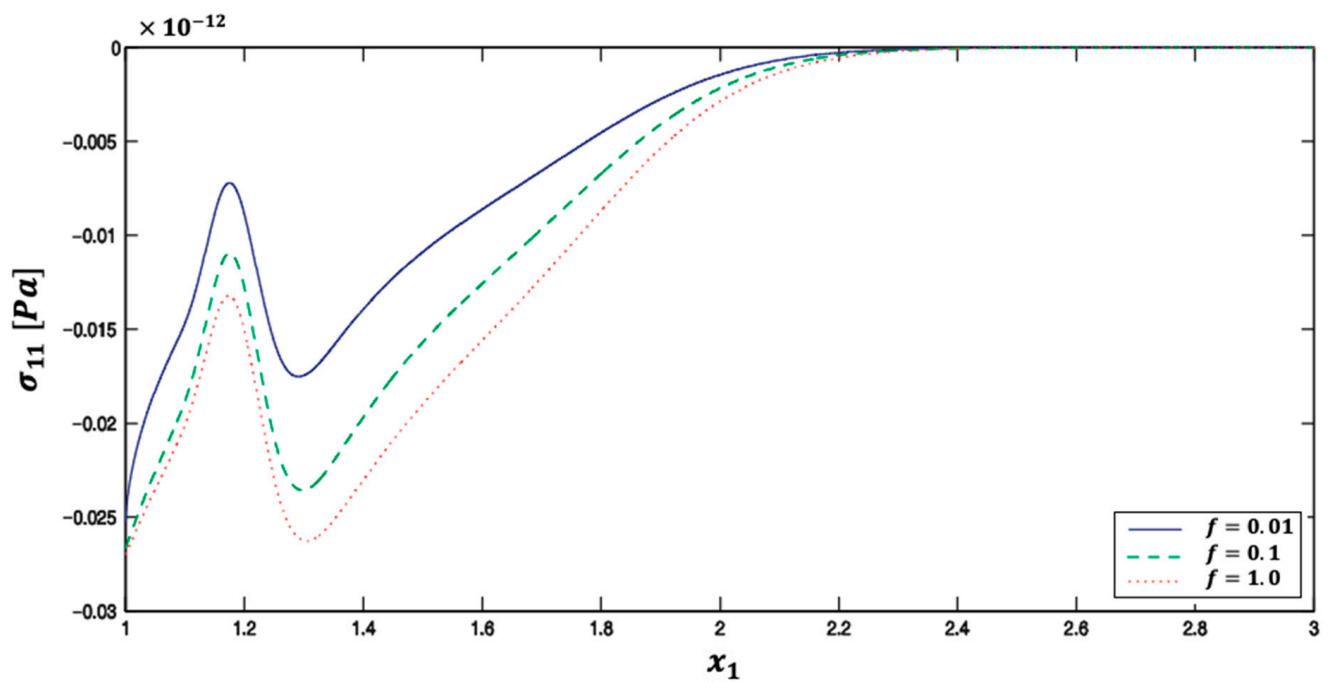


Figure 10. Total force-stress σ_{11} distribution on x_1 -axis for various piezoelectric parameter f values.

Figure 11 shows the total force-stress σ_{12} distribution for various values of piezoelectric parameter f .

From Figure 12, The total force-stress σ_{22} increases, decreases, and then tend toward zero as x_1 tends toward infinity. It is also shown that the values of total force-stress σ_{22} almost coincide at the different values of piezoelectric parameter f , except for the interval $1.25 < x_1 < 2.20$, where we find that the total force-stress σ_{12} decreases with an increase of piezoelectric parameter f .

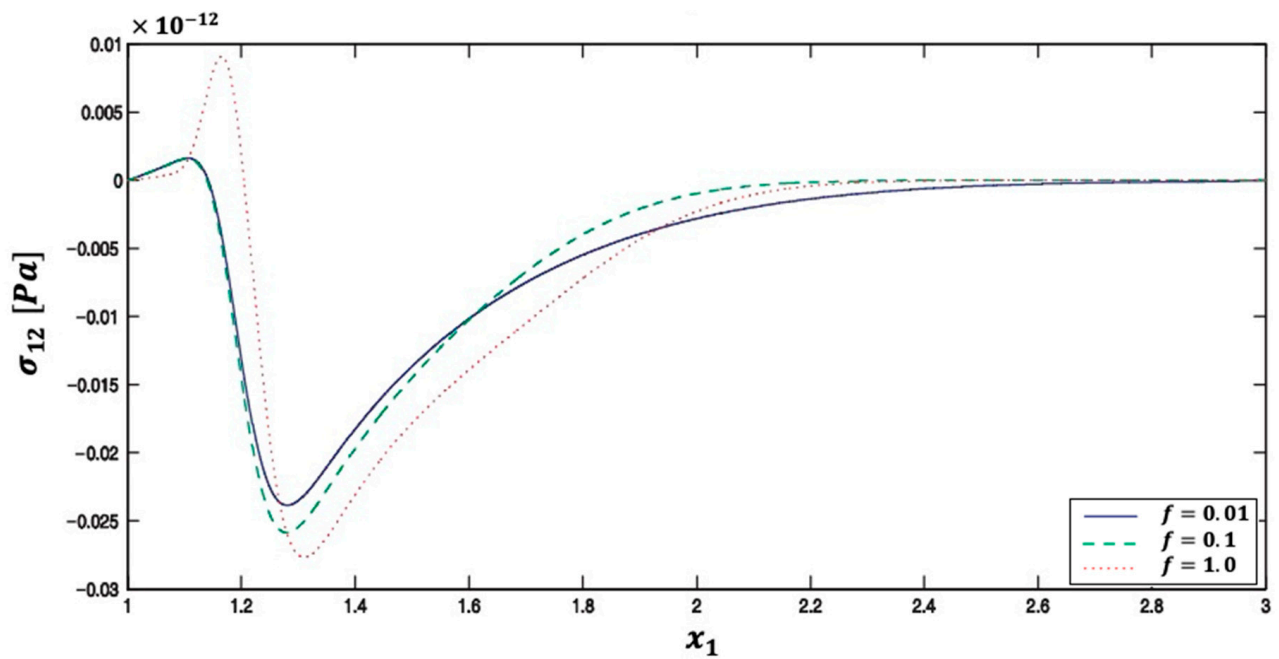


Figure 11. Total force-stress σ_{12} distribution on x_1 -axis for various piezoelectric parameter f values.

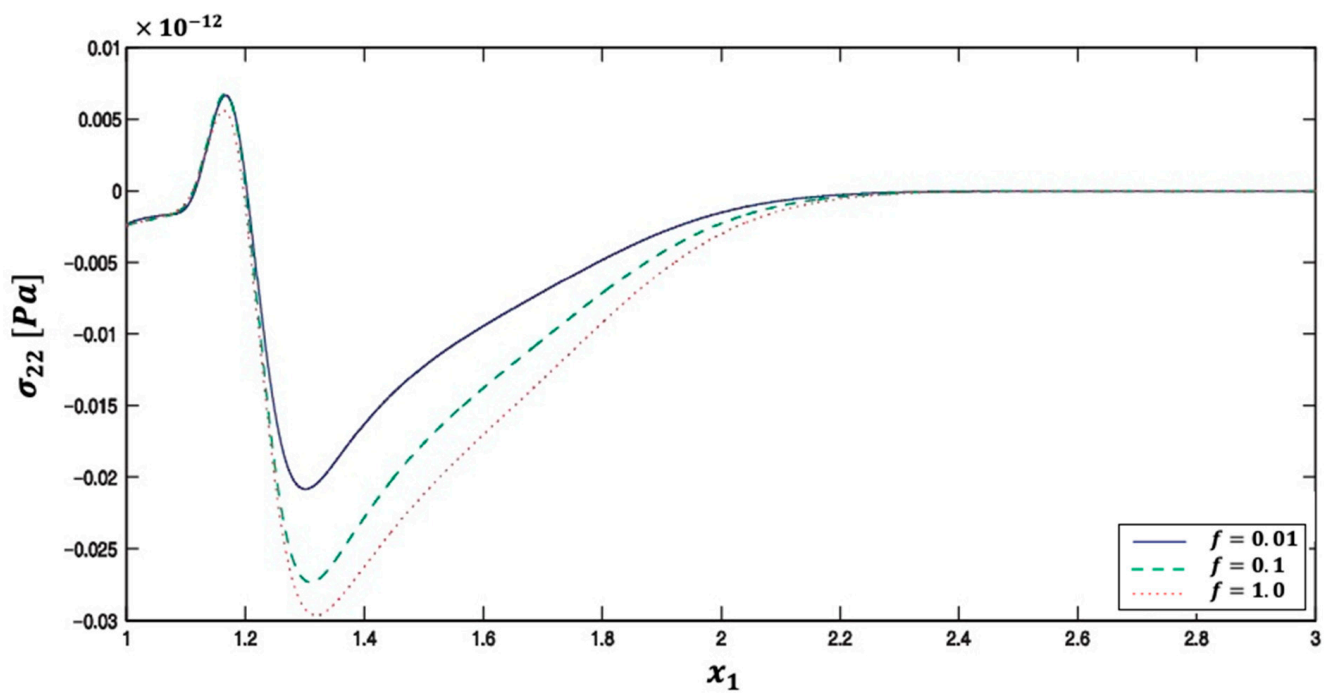


Figure 12. Total force-stress σ_{22} distribution on x_1 -axis for various piezoelectric parameter f values.

From Figure 13, it is obvious that the total force-stress σ_{22} increases, decreases, and then tends toward zero as x_1 tends toward infinity. It is also clear that the total force-stress σ_{11} decreases with small values of length scale parameter l and then increases with large values of length scale parameter l .

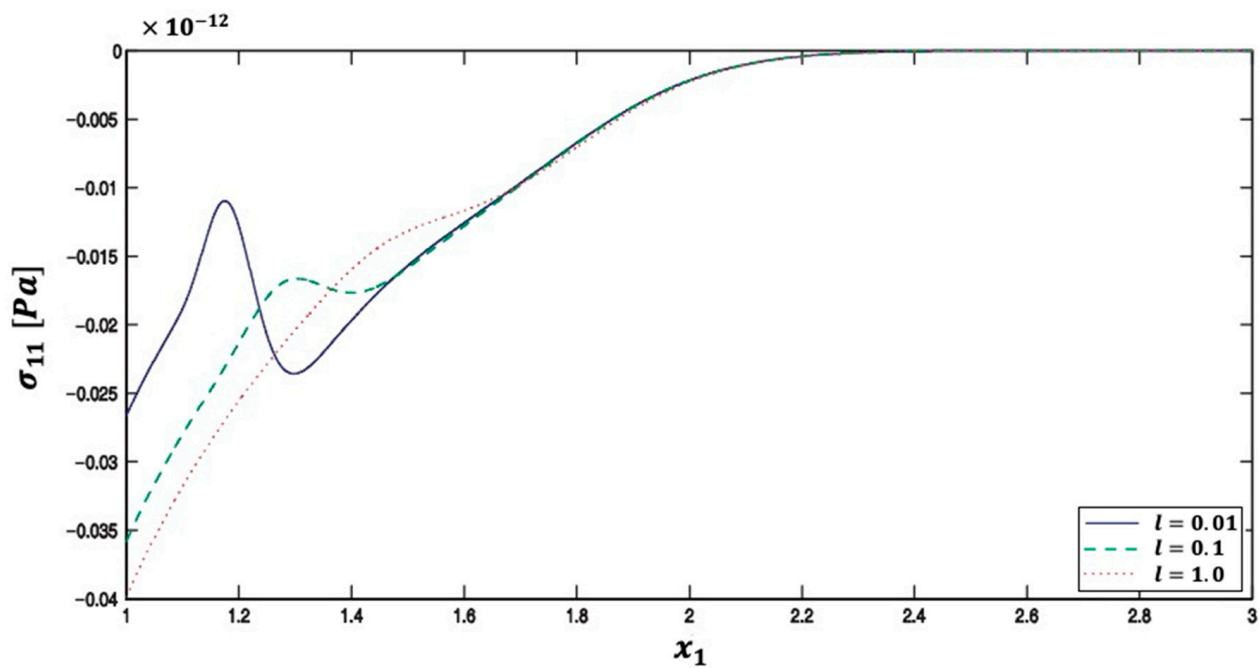


Figure 13. Total force-stress σ_{11} distribution on x_1 -axis for various length scale l values.

From Figure 14, it is obvious that the total force-stress σ_{12} increases, decreases, and then tends toward zero as x_1 tends toward infinity. It is also clear that the total force-stress σ_{12} decreases with small values of length scale parameter l and then increases with large values of length scale parameter l .

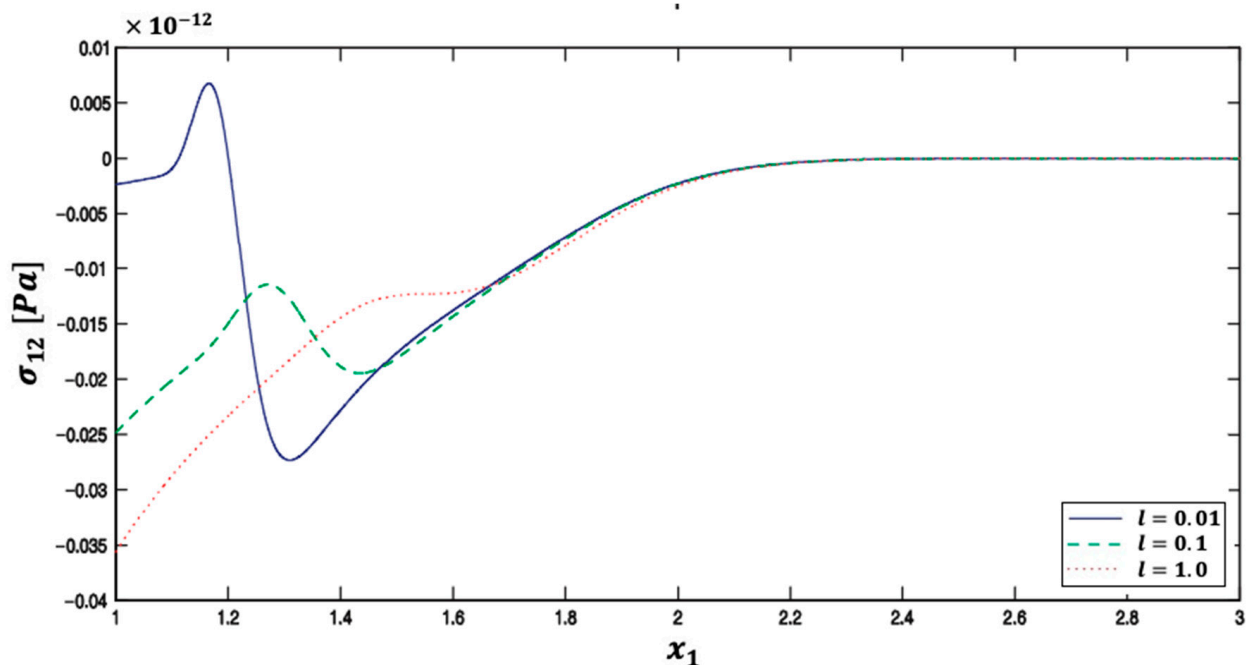


Figure 14. Total force-stress σ_{12} distribution on x_1 -axis for various length scale l values.

From Figure 15, it is concluded that the total force-stress σ_{22} along the x_1 -axis increases for the small values of x_1 with an increasing of length scale parameter l . It is clear that the total force-stress σ_{12} decreases and increases with large values of x_1 and tends toward zero as x_1 tends toward infinity.

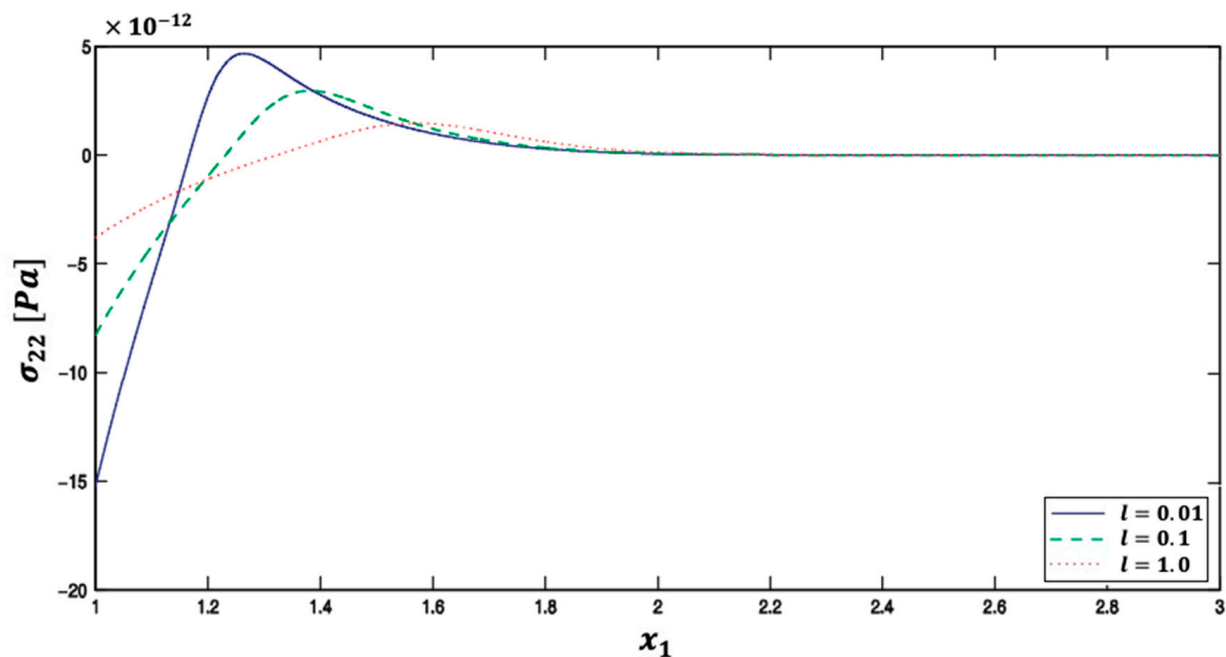


Figure 15. Total force-stress σ_{22} distribution on x_1 -axis for various length scale l values.

6. Conclusions

A new BEM model for temperature- and size-dependent fractional thermoelastic problems in smart nanomaterials is introduced.

A new efficient BEM methodology is developed for treating temperature-dependent and size-dependent thermoelastic problems in smart nanomaterials.

The BEM efficiency has been shown by the usage of the SCAS-GMRES, which minimizes memory needs and processing time.

The suggested model includes thermoelastic and piezoelectric impacts, which allows us to explain the differences between temperature-dependent smart nanomaterials, temperature-independent smart nanomaterials, temperature-dependent non-smart nanomaterials, and temperature-independent non-smart nanomaterials.

The numerical data are plotted to show the impacts of the fractional order parameter, temperature, and size on the total force-stresses.

The computational effectiveness of the suggested methodology has been established.

The proposed BEM approach has been shown to be valid and accurate.

We can conclude from current study that our proposed BEM technique is practicable, feasible, effective, and superior to FDM or FEM.

The proposed methodology can be utilized to examine a wide range of thermoelastic problems in smart nanomaterials that are temperature and size dependent.

It can be argued that our research has a wide range of applications, including shape memory alloys, environmental sensors, photovoltaic cells, nanoceramics, sunscreens, air purifiers, food packaging, flame retardants, antibacterial cleansers, filters, smart coatings, and thin films.

Recent numerical calculations for issues with smart nanomaterials may be of interest to nanophysicists, nanochemists, and nanobiologists, in addition to mathematicians with expertise in nanotechnology, quantum computing, artificial intelligence, and optogenetics.

Funding: This research was funded by the Deanship of Scientific Research at Umm Al-Qura University, grant number 22UQU4340548DSR17. The APC was funded by the Deanship of Scientific Research at Umm Al-Qura University.

Institutional Review Board Statement: Not applicable.

Informed Consent Statement: Not applicable.

Data Availability Statement: All data generated or analyzed during this study are included in this published article.

Acknowledgments: The author would like to thank the Deanship of Scientific Research at Umm Al-Qura University for supporting this work, grant code 22UQU4340548DSR17.

Conflicts of Interest: The author declares no conflict of interest.

Nomenclature

\bar{a}	Coefficient of thermal expansion	F_α	Body force vector
a	Fractional-order parameter	F^*	Point force kernel function
$\delta_{\alpha\beta}$	Kronecker delta function	f	Piezoelectric coefficient
λ & μ	Lamé elastic constants	$J(\tau)$	Non-Gaussian temporal profile
ρ_E	Volume electric charge density	J_0	Total energy intensity
η	Couple-stress parameter	k	Thermal conductivity
$\sigma_{\alpha\beta}$	Total force-stress tensor	k_α	Mean curvature vector
$\sigma_{(\alpha\beta)}$	Symmetric force-stress tensor	$k_{\alpha\beta}$	Pseudo mean curvature tensor
$\sigma_{[\alpha\beta]}$	Skew-symmetric force-stress tensor	l	The material length scale parameter
τ	Time	M_i	True couple-stress vector
τ_1	Laser pulse time characteristic	M_{kj}	Pseudo couple-stress tensor
φ	Electric potential	m	Couple-traction
Ω	Rotation	n_α	Outward unit normal vector
A	Non-symmetric dense matrix	P_α	Polarization of piezoelectric material
B	Known boundary values vector	Q	External heat source
C^*	Point couple kernel function	Q^*	Point heat source kernel function
D_α	Electric displacement	q	Normal flux
d	Normal electric displacement	q_α	Heat flux vector
E	Young's modulus	R	Irradiated surface absorptivity
E_α	Electric field	R^*	Point electrical source kernel function
$e_{\alpha\beta}$	2D permutation symbol	T	Temperature
e_{ijk}	3D Levi-Civita permutation symbol	t_I	Generalized tractions
e	Electric permittivity	t_α	Force-traction vector
e_r	Relative permittivity	u_α	Displacement vector
e_0	Vacuum permittivity	ν	Poisson ratio
X	Unknown boundary values vector		

References

1. Youssef, H.M.; Al-Lehaibi, E.A.N. 2-D mathematical model of hyperbolic two-temperature generalized thermoelastic solid cylinder under mechanical damage effect. *Arch. Appl. Mech.* **2022**, *92*, 945–960. [\[CrossRef\]](#)
2. Youssef, H.M.; Al-Lehaibi, E.A.N. General generalized thermoelasticity theory (GGTT). *J. Therm. Anal. Calorim.* **2023**, *148*, 5917–5926. [\[CrossRef\]](#)
3. Youssef, H.M.; Al-Lehaibi, E.A.N. The photothermal interaction of a semiconducting solid sphere based on three Green-Naghdi theories due to the fractional-order strain and ramp-type heating. *Mech. Time-Depend. Mater.* **2022**, 1–20. [\[CrossRef\]](#)
4. Othman, M.I.A.; Fekry, M. Effect of Magnetic field on generalized thermo-viscoelastic diffusion medium with voids. *Int. J. Struct. Stab. Dyn.* **2016**, *16*, 1550033. [\[CrossRef\]](#)
5. Othman, M.I.A.; Fekry, M.; Marin, M. Plane Waves in Generalized Magneto-thermo-viscoelastic Medium with Voids under the Effect of Initial Stress and Laser Pulse Heating. *Struct. Eng. Mech.* **2020**, *73*, 621–629.
6. Othman, M.I.A.; Fekry, M. Effect of Rotation and Gravity on Generalized Thermo-viscoelastic Medium with Voids. *Multidiscip. Model. Mater. Struct.* **2018**, *14*, 322–338. [\[CrossRef\]](#)
7. Ghanbari, J.; Naghdabadi, R. Multiscale nonlinear constitutive modeling of carbon nanostructures based on interatomic potentials. *CMC-Comput. Mater. Contin.* **2009**, *10*, 41–64.
8. Chakrabarty, A.; Çağın, T. Computational studies on mechanical and thermal properties of carbon nanotube based nanostructures. *CMC-Comput. Mater. Contin.* **2008**, *7*, 167–190.
9. Cha, S.N.; Seo, J.S.; Kim, S.M.; Kim, H.J.; Park, Y.J.; Kim, S.-W.; Kim, J.M. Sound-driven piezoelectric nanowire-based nanogenerators. *Adv. Mater.* **2010**, *22*, 4726–4730. [\[CrossRef\]](#)
10. Voiculescu, I.; Nordin, A.N. Acoustic wave based MEMS devices for biosensing applications. *Biosens. Bioelectron.* **2012**, *33*, 1–9. [\[CrossRef\]](#)

11. Shin, D.; Urzhumov, Y.; Jung, Y.; Kang, G.; Baek, S.; Choi, M.; Park, H.; Kim, K.; Smith, D.R. Broadband electromagnetic cloaking with smart metamaterials. *Nat. Commun.* **2012**, *3*, 1213. [\[CrossRef\]](#)
12. Zhang, S.; Gu, B.; Zhang, H.; Feng, X.Q.; Pan, R.; Alamusi; Hu, N. Propagation of Love waves with surface effects in an electrically-shorted piezoelectric nano film on a half-space elastic substrate. *Ultrasonics* **2016**, *66*, 65–71. [\[CrossRef\]](#)
13. Akyildiz, I.F.; Jornet, J.M. Electromagnetic wireless nanosensor networks. *Nano Commun. Networks* **2010**, *1*, 3–19. [\[CrossRef\]](#)
14. He, J.; Qi, X.; Miao, Y.; Wu, H.L.; He, N.; Zhu, J.-J. Application of smart nanostructures in medicine. *Nanomedicine* **2010**, *5*, 1129–1138. [\[CrossRef\]](#)
15. Al-Hossain, A.Y.; Farhoud, F.A.; Ibrahim, M. The mathematical model of reflection and refraction of plane quasi-vertical transverse waves at interface nanocomposite smart material. *J. Comput. Theor. Nanosci.* **2011**, *8*, 1193–1202.
16. Zhu, L.L.; Zheng, X.J. Stress field effects on phonon properties in spatially confined semiconductor nanostructures. *CMC-Comput. Mater. Contin.* **2010**, *18*, 301–320.
17. Danl, Y.; Huynen, I.; Bailly, C. Thin smart multilayer microwave absorber based on hybrid structure of polymer and carbon nanotubes. *Appl. Phys. Lett.* **2012**, *100*, 213105. [\[CrossRef\]](#)
18. Ezzat, M.A. State space approach to unsteady two-dimensional free convection flow through a porous medium. *Can. J. Phys.* **1994**, *72*, 311–317. [\[CrossRef\]](#)
19. Ezzat, M.; Zakaria, M.; Shaker, O.; Barakat, F. State space formulation to viscoelastic fluid flow of magnetohydrodynamic free convection through a porous medium. *Acta Mech.* **1996**, *119*, 147–164. [\[CrossRef\]](#)
20. Ezzat, M.A. Free convection effects on perfectly conducting fluid. *Int. J. Eng. Sci.* **2001**, *39*, 799–819. [\[CrossRef\]](#)
21. Hadjesfandiari, A.R. Size-dependent piezoelectricity. *Int. J. Solids Struct.* **2013**, *50*, 2781–2791. [\[CrossRef\]](#)
22. Fahmy, M.A. A new BEM modeling algorithm for size-dependent thermopiezoelectric problems in smart nanostructures. *CMC-Comput. Mater. Contin.* **2021**, *69*, 931–944. [\[CrossRef\]](#)
23. Fahmy, M.A.; Almeahmadi, M.M.; Al Subhi, F.M.; Sohail, A. Fractional boundary element solution of three-temperature thermo-electric problems. *Sci. Rep.* **2022**, *12*, 6760. [\[CrossRef\]](#) [\[PubMed\]](#)
24. Fahmy, M.A. 3D boundary element model for ultrasonic wave propagation fractional order boundary value problems of functionally graded anisotropic fiber-reinforced plates. *Fractal Fract.* **2022**, *6*, 247. [\[CrossRef\]](#)
25. Fahmy, M.A. Boundary element modeling of fractional nonlinear generalized photothermal stress wave propagation problems in FG anisotropic smart semiconductors. *Eng. Anal. Bound. Elem.* **2022**, *2022*, 665–679. [\[CrossRef\]](#)
26. Fahmy, M.A.; Alsulami, M.O. boundary element and sensitivity analysis of anisotropic thermoelastic metal and alloy discs with holes. *Materials* **2022**, *15*, 1828. [\[CrossRef\]](#)
27. Darrall, B.T.; Hadjesfandiari, A.R.; Dargush, G.F. Size-dependent piezoelectricity: A 2D finite element formulation for electric field-mean curvature coupling in dielectrics. *Eur. J. Mech. -A/Solids* **2015**, *49*, 308–320. [\[CrossRef\]](#)
28. Fahmy, M.A. Three-Dimensional Boundary Element Strategy for Stress Sensitivity of Fractional-Order Thermo-Elastoplastic Ultrasonic Wave Propagation Problems of Anisotropic Fiber-Reinforced Polymer Composite Material. *Polymers* **2022**, *14*, 2883. [\[CrossRef\]](#)
29. Cattaneo, C. Sur une forme de l'équation de la Chaleur Elinant le Paradox d'une Propagation Instantanc. In *Comptes Rendus de l'Académie des Sciences*; Gauthier-Villars: Paris, France, 1958; Volume 247, pp. 431–433.
30. Carslaw, H.S.; Jaeger, J.C. *Conduction of Heat in Solids*; Clarendon Press: Oxford, UK, 1959.
31. Fahmy, M.A. A Nonlinear Fractional BEM Model for Magneto-Thermo-Visco-Elastic Ultrasound Waves in Temperature-Dependent FGA Rotating Granular Plates. *Fractal Fract.* **2023**, *7*, 214. [\[CrossRef\]](#)
32. Wrobel, L.C. *The Boundary Element Method: Applications in Thermo-Fluids and Acoustics*; John Wiley & Sons: Hoboken, NJ, USA, 2002.
33. Hematiyan, M.R. Exact transformation of a wide variety of domain integrals into boundary integrals in boundary element method. *Commun. Numer. Methods Eng.* **2008**, *24*, 1497–1521. [\[CrossRef\]](#)
34. Hematiyan, M.R. A general method for evaluation of 2D and 3D domain integrals without domain discretization and its application in BEM. *Comput. Mech.* **2007**, *39*, 509–520. [\[CrossRef\]](#)
35. Khosravifard, A.; Hematiyan, M.R. A new method for meshless integration in 2D and 3D Galerkin meshfree methods. *Eng. Anal. Bound. Elem.* **2010**, *34*, 30–40. [\[CrossRef\]](#)
36. Liu, G.R.; Gu, Y.T. *An Introduction to Meshfree Methods and Their Programming*; Springer: New York, NY, USA, 2005.
37. Hadjesfandiari, A.R.; Dargush, G.F. Fundamental solutions for isotropic size-dependent couple stress elasticity. *Int. J. Solids Struct.* **2013**, *50*, 1253–1265. [\[CrossRef\]](#)
38. Hajesfandiari, A.; Hadjesfandiari, A.R.; Dargush, G.F. Boundary element formulation for plane problems in size-dependent piezoelectricity. *Int. J. Numer. Methods Eng.* **2016**, *108*, 667–694. [\[CrossRef\]](#)
39. Hajesfandiari, A.; Hadjesfandiari, A.R.; Dargush, G.F. Boundary element formulation for steady state plane problems in size-dependent thermoelasticity. *Eng. Anal. Bound. Elem.* **2017**, *82*, 210–226. [\[CrossRef\]](#)
40. Fahmy, M.A. A new boundary element algorithm for modeling and simulation of nonlinear thermal stresses in micropolar FGA composites with temperature-dependent properties. *Adv. Model. Simul. Eng. Sci.* **2021**, *8*, 6. [\[CrossRef\]](#)
41. Abouelregal, A.E.; Fahmy, M.A. Generalized Moore-Gibson-Thompson thermoelastic fractional derivative model without singular kernels for an infinite orthotropic thermoelastic body with temperature-dependent properties. *ZAMM J. Appl. Math. Mech.* **2022**, *102*, e202100533. [\[CrossRef\]](#)

42. Suramwar, N.V.; Thakare, S.R.; Khaty, N.T. One pot synthesis of copper nanoparticles at room temperature and its catalytic activity. *Arab. J. Chem.* **2016**, *9*, S1807–S1812. [[CrossRef](#)]
43. Xu, Z.; Alonso, J.J.; Darve, E. A numerically stable communication avoiding S-step GMRES algorithm. *arXiv* **2023**, arXiv:2303.08953. [[CrossRef](#)]
44. Shao, X.-H.; Kang, C.-B. Modified DTS iteration methods for spatial fractional diffusion equations. *Mathematics* **2023**, *11*, 931. [[CrossRef](#)]
45. She, Z.-H.; Qiu, L.-M.; Qu, W. An unconditionally convergent RSCSCS iteration method for Riesz space fractional diffusion equations with variable coefficients. *Math. Comput. Simul.* **2023**, *203*, 633–646. [[CrossRef](#)]
46. Sladek, J.; Sladek, V.; Repka, M.; Tan, C.L. Size dependent thermo-piezoelectricity for in-plane cracks. *Key Eng. Mater.* **2019**, *827*, 147–152. [[CrossRef](#)]
47. Yu, Y.J.; Tian, X.G.; Liu, X.R. Size-dependent generalized thermoelasticity using Eringen's nonlocal model. *Eur. J. Mech. A/Solids* **2015**, *51*, 96–106. [[CrossRef](#)]

Disclaimer/Publisher's Note: The statements, opinions and data contained in all publications are solely those of the individual author(s) and contributor(s) and not of MDPI and/or the editor(s). MDPI and/or the editor(s) disclaim responsibility for any injury to people or property resulting from any ideas, methods, instructions or products referred to in the content.